Analyst

ROYAL SOCIETY OF CHEMISTRY

PAPER

View Article Online
View Journal | View Issue

Cite this: *Analyst*, 2025, **150**, 2809

FTIR-based machine learning for prediction of malignant transformation in oral epithelial dysplasia

Rong Wang, *[a] Roya Sabzian,[b] Tanya M. Gibson[c] and Yong Wang [a]

Oral squamous cell carcinoma (OSCC) is an aggressive cancer with a poor prognosis. Oral epithelial dysplasia (OED) is a precancerous lesion associated with an increased risk of malignant transformation (MT) into OSCC. However, current histopathological methods for diagnosing OED are subjective and ineffective in assessing MT risk. FTIR provides a comprehensive biochemical profile of tissues, known as "biomolecular fingerprinting". Previously we developed an FTIR-based OSCC-Benign classifier that accurately distinguishes OSCC from benign tissue. In this study, we evaluated whether this classifier could also predict MT risk in OED. Thirty OED patient biopsies with documented MT outcomes were analyzed, including 12 with and 18 without MT. FTIR images were acquired from six regions of interest (ROIs) per tissue section, yielding an average epithelial spectrum for each ROI, and a total of 180 spectra for model evaluation. The OSCC-Benign classifier achieved an accuracy of 81.7% with an F1 score of 0.77 at the ROI level, and an accuracy of 83.3% with an F1 score of 0.8 at the biopsy level in predicting MT in OED. Our findings suggest that OEDs with biomolecular fingerprints similar to OSCC carry a higher risk of MT, while those resembling benign tissue carry a lower risk, providing new insight into the malignant transformation process. In summary, the FTIR-based machine learning approach outperforms traditional histopathology in predicting MT risk in OED, potentially offering a quantitative and objective tool for clinical diagnosis.

Received 30th January 2025,
Accepted 8th May 2025

DOI: 10.1039/d5an00117j

rsc.li/analyst

Introduction

Oral cancer refers to a subgroup of head and neck malignancies that affect various intra-oral sites, including the lips, tongue, gingiva, floor of the mouth, and buccal mucosa. It poses a significant global health concern, with an estimated 377 713 new cases and 177 757 deaths reported in 2020, predominantly in low- and middle-income countries.[1] More than 90% of oral cancers are oral squamous cell carcinoma (OSCC). Despite the accessibility of the oral cavity for clinical examination and advancements in therapeutic strategies, the overall five-year survival rate for OSCC remains low, ranging from 50% to 60%. Early detection is critical for improving patient prognosis and survival outcomes.[2,3]

Oral carcinogenesis is a highly complex, multifactorial, and multistep process. It often begins with benign hyperplasia/hyperkeratosis, progressing to oral epithelial dysplasia (OED), carcinoma *in situ*, and finally invasive OSCC.[4] OED, a microscopically diagnosed precancerous lesion, is associated with an increased risk of malignant transformation (MT) into OSCC. It is characterized by cytological and architectural alterations that disrupt the normal maturation and stratification of the epithelium. An OED can be graded as mild, moderate, or severe based on the three-tier classification system established by the World Health Organization (WHO).[5] It has been reported that the likelihood of MT varied by OED grade, with an estimated rate of 7%–50% for severe, 3%–30% for moderate, and <5% for mild OED.[6–8] Although these histological grades statistically correlate with clinical outcomes, the WHO's gold standard diagnostic system is subjective and ineffective in predicting MT risk in individual OED patients.[9,10] To overcome these limitations, researcher have proposed integrating clinical and molecular biomarkers into the diagnostic process; however, none have achieved the desired clinical effectiveness.[10,11]

Fourier transform infrared (FTIR) spectroscopy is a versatile analytical technique used to characterize molecular structures by analyzing how chemical bonds interact with infrared radiation. This technique generates a unique spectral

[a]*Department of Oral and Craniofacial Sciences, School of Dentistry, University of Missouri Kansas City, Kansas City, MO, USA. E-mail: wangrong@umkc.edu, wangyo@umkc.edu; Tel: +816-235-2176*
[b]*Department of Restorative Dentistry, Rutgers School of Dental Medicine, Newark, NJ, USA. E-mail: Rs2430@rsdm.rutgers.edu*
[c]*Department of Oral Pathology, Radiology & Medicine, School of Dentistry, University of Missouri Kansas City, Kansas City, MO, USA. E-mail: gibsontm@umkc.edu*

"fingerprint" that provides qualitative and quantitative insights into the biochemical composition of a specimen, including proteins, nucleic acids, lipids, and carbohydrates.[12,13] When combined with light microscopy, FTIR imaging enables spatially resolved biomolecular analysis producing a three-dimensional hyperspectral dataset. Due to its label-free, non-invasive, and highly sensitive nature, FTIR spectroscopy and imaging techniques have been explored for the detection and diagnosis of various cancers.[14–17] FTIR imaging generates high-dimensional data, often requiring multivariate chemometric and machine learning methods for data analysis and interpretation.[17]

In a previous study, we applied FTIR imaging and machine learning to differentiate between OSCC, OED and benign (hyperkeratosis) oral biopsy tissues. We developed three supervised discriminant models – partial least squares discriminant analysis (PLSDA), support vector machines discriminant analysis (SVMDA), and extreme gradient boosting discriminant analysis (XGBDA) – to discriminate OSCC from benign tissues. Using 10-fold Venetian blinds cross-validation, we reported 100% sensitivity and specificity for the PLSDA model, compared to 95% sensitivity and 96% specificity for the SVMDA and XGBDA models.[18] These preliminary results were very encouraging, though the potential risk for overfitting remains a concern due to the limited sample size. Exploratory analysis of the OED biopsy samples (hereafter referred to as biopsies) revealed partial spectral overlap with both OSCC and benign tissues. When evaluated using the OSCC-Benign PLSDA model, some OED spectra were classified as OSCC-like, while others Benign-like. Since clinical outcomes for these OED biopsies were previously unknown, we hypothesized that OED spectra classified as OSCC-like indicate a higher risk of MT, whereas those classified as Benign-like suggest a lower risk.

In the current study, to test this hypothesis, we analyzed 30 OED patient biopsies with documented clinical outcomes, including 12 that underwent MT and 18 that did not. The original histopathological diagnoses of these biopsies were verified by a collaborating oral pathologist and used as the "ground truth" for validation. FTIR images were acquired from six regions of interest (ROIs) per biopsy, and the corresponding average epithelial spectra were computed, resulting in a dataset of 180 spectra labeled according to the verified MT outcomes. Using this OED FTIR dataset as a test set, we assessed the feasibility and effectiveness of the OSCC-Benign PLSDA model for predicting MT risk in OED. In comparison, we also trained a new PLSDA model using the OED FTIR dataset itself and evaluated its performance using cross-validation.

Experimental

Fig. 1 illustrates the schematic of the experimental workflow, which is described in detail in the following sections. All experiments were performed in accordance with the Ethical Principles and Guidelines for the Protection of Human Subjects of Research, and were approved by the Institutional Review Board of the University of Missouri–Kansas City (UMKC) under project number 2087842. Patient identifiers were removed prior to experimentation to ensure privacy and confidentiality.

Patient biopsy identification and sample preparation

The patient database in the UMKC School of Dentistry Pathology Department was searched to identify suitable biopsy samples for the study. OED patient biopsies with documented

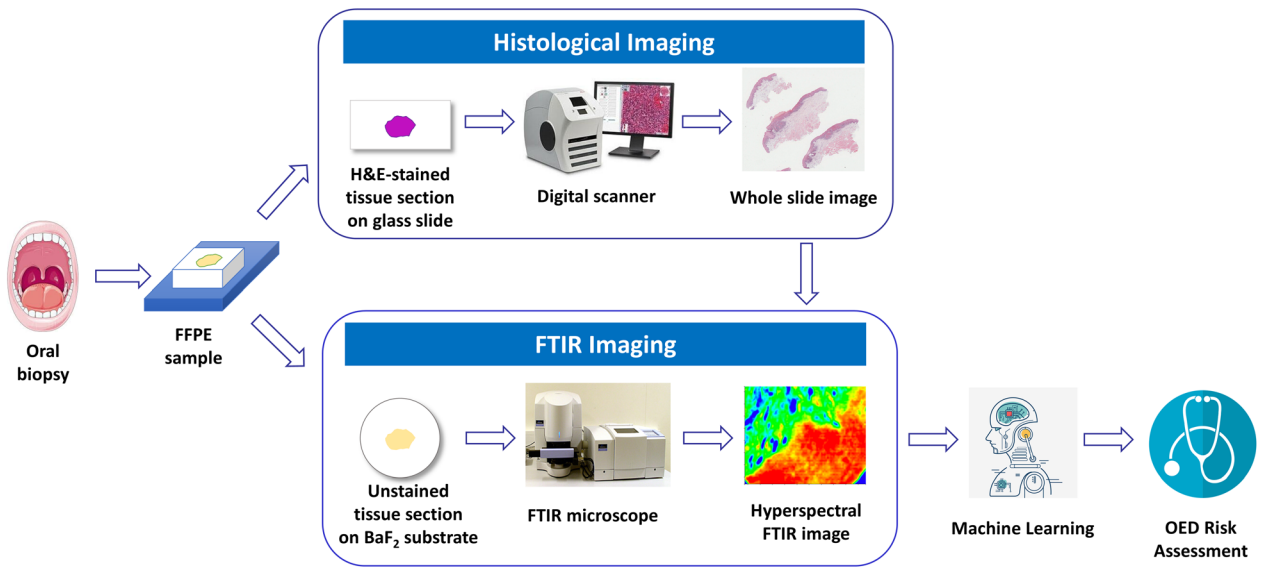

Fig. 1 Schematic illustration of the experimental workflow. Two consecutive thin sections of FFPE (formalin-fixed paraffin-embedded) oral biopsy tissues were subject to H&E staining and FTIR imaging. Machine learning analyses were performed on FTIR spectra from the OED biopsies to assess their MT risk.

MT were selected based on an initial diagnosis of dysplasia followed by a subsequent OSCC diagnosis in the same patients. OED biopsies without MT were selected based on an initial dysplastic diagnosis followed by a later diagnosis that did not progress to OSCC. Since the timeline for malignant transformation varies, definitive determination of OED cases without MT remains challenging. Considering the reported average transformation time of 1.82 ± 1.55 years for OED,[19] we used a practical selection criterion requiring a minimum two-year interval between the initial and follow-up diagnoses for cases without MT. Consequently, 30 formalin-fixed paraffin-embedded OED blocks were identified from the Pathology Department, including 12 with MT from 9 patients and 18 without MT from 17 patients. Four patients had multiple OED diagnoses over time before the final diagnosis. These biopsies were included in our investigation as independent samples and are discussed in groups by patients. De-identified demographic and diagnostic information was provided by the collaborating oral pathologist and summarized in Table 1.

Two 4-micron-thick sections were cut from each block using a microtome (Leica RM2125, RTS, Leica Biosystems Inc., Buffalo Grove, IL, USA). One section was affixed onto a positively charged glass slide (Cat. No.: 22034979, Fisher Scientific, Waltham, MA, USA) for Hematoxylin and Eosin (H&E) staining and histological evaluation. The adjacent section was placed on an IR transparent BaF_2 substrate measuring 25 × 2 mm (REFLEX Analytical Corporation, Ridgewood, NJ, USA) for FTIR imaging. The H&E-stained sections were digitally scanned at ×40 magnification using a Leica Aperio CS2 digital scanner (Leica Biosystems W. Lake Cook Road, Deer Park, IL, USA) and sent to our collaborating oral pathologist for verification. Then the digital H&E images were manually annotated for the dysplastic regions using the open-source software QuPath (v0.4.0) and used as references for ROI selection during FTIR imaging. The biopsy tissue sections on the BaF_2 substrate underwent deparaffinization by immersion in histological grade xylene (CAS number 1330-20-7, Sigma-Aldrich, St Louis, MO, USA) three times for five minutes each at room temperature. The deparaffinized sections were air-dried and stored in a vacuum desiccator for FTIR imaging within a week.

FTIR image acquisition

FTIR images were acquired in transmission mode using a PerkinElmer FTIR Spectrum Spotlight imaging system (Spectrum one, Spotlight 300, PerkinElmer, Waltham, MA, USA). The Spotlight 300 imaging system is equipped with a dual-mode detector featuring a 1 × 16 narrow band mercury cadmium telluride (MCT) array and 100 μm medium band MCT single point detector, operating at liquid nitrogen temperature. The FTIR image acquisition parameters were set as follows: spectral resolution 4 cm^{-1}, spectral range 4000–950 cm^{-1}, pixel resolution 6.25 μm, and co-adding number 16 per pixel. First, a survey image was generated using the built-in light microscope in the FTIR Spotlight system for the tissue section. Subsequently, more than six ROIs in the size of 400 μm × 100 μm (64 × 16 pixels) were defined on the survey image, in reference to the annotated digital H&E image. The ROIs were selected to encompass the basal epithelium and adjacent stroma, while avoiding areas with poor structural integrity. Before acquiring FTIR images for each ROI, a background spectrum was obtained from a clean area of the substrate outside the tissue section for background correction. FTIR image acquisition was carried out using the Spectrum IMAGE software by PerkinElmer.

Data analysis

The same spectral preprocessing, outlier removal, and clustering procedures used in the development of the OSCC-Benign models in our previous study were used in the current study and are briefly described below.[18] The data analysis and machine learning modeling were performed using the Eigenvector PLS_Toolbox 9.3 and MIA_Toolbox 3.1 (Eigenvector research incorporated, Inc., Manson, WA, USA) in MATLAB (R2020b, MathWorks).

Spectral preprocessing

Raw hyperspectral images were preprocessed as follows: 1, transmission to absorbance conversion ($A = \log(1/T)$); 2, fingerprint region selection (1800–950 cm^{-1}); 3, Savitzky–Golay smoothing (order = 2, window = 13 pt, tails: polyinterp); 4, EMSC (extended multiplicative signal correction) for light-scattering; 5, baseline correction using automated weighted least squares (order = 3); and 6, vector normalization (length = 1). During model training, validation and testing, a second derivative transformation (order = 2, window = 7 pt) was further applied to the input spectral data to enhance model performance.

Outlier removal

Outliers may be present in the pixel-level spectral data, particularly from areas with compromised tissue quality or integrity. To address this, unsupervised principal component analysis (PCA) was performed after spectral preprocessing to identify and remove outliers. PCA transforms the original coordinate system into a new one defined by principal components (PCs) that capture the most significant variance in the dataset. For each ROI image dataset, a Reduced Hotelling's T^2 *versus* Reduced Q residual scatter plot was generated. Spectra with values exceeding 1 in either Reduced Hotelling's T^2 or Reduced Q residual were flagged, examined, and subsequently removed to ensure data integrity.

Representative spectra extraction

Each ROI typically contain both epithelial and stromal tissues. To distinguish FTIR spectra of different tissue components, unsupervised hierarchical cluster analysis (HCA) was employed to cluster pixel-level spectra in each ROI using Ward's method.[20] The histological identity of each cluster was determined by referencing the corresponding H&E-stained section. Then the average spectra from epithelial clusters in each ROI were extracted and used as the representative spectra for subsequent analyses. Not all acquired ROI images yielded high

Table 1 Deidentified demographic and diagnostic information for the thirty OED patient biopsies and ROI-level risk prediction by the OSCC-Benign PLSDA model

Biopsy information			Initial diagnosis		Follow-up diagnosis		Model prediction
ID	Patient birth year	Sex	Clinical description	Histological diagnosis Location Month/year	Clinical description	Histological diagnosis Location Month/year	ROI-level
OED biopsies with MT							
05	**1930**	**F**	**Leukoplakia, ulceration**	**Mod to sev OED** **Lateral/ventral Tongue** **10/2014**	**Leukoplakia, ulceration**	**Mod to well diff. SCC** **Lateral tongue** **03/2015**	**6/6 low risk**
06	1945	F	Not given	VHK w mod OED Buccal vestibule 10/2014	*erythro*-Leukoplakia	Sf-invasive SCC Retromolar region 08/2019	5/6 high risk 1/6 low risk
94	1945	F	Not given	HK & acan w mod OED Retromolar pad area 09/2018	*erythro*-Leukoplakia	Sf-invasive SCC Retromolar region 08/2019	6/6 high risk
42	1952	F	*erythro*-Leukoplakia	Mod to sev OED Palatal papilla 09/2016	*erythro*-Leukoplakia	Mod to well diff. SCC Buccal mucosa 04/2018	5/6 high risk 1/6 low risk
46	1932	F	Granular tissue mass	Atyp EH w OED Buccal mucosa 12/2016	Raised dense tissue	Well diff. SCC Edentulous ridge & buccal mucosa 03/2017	6/6 high risk
51	1939	M	Mixed *erythro*-leukoplakia	Atyp EH w sev OED Anterior maxilla 02/2017	Ulceration	Mod diff. SCC Palatal mucosa & gingival margin 01/2018	5/6 high risk 1/6 low risk
55	1939	M	*erythro*-Leukoplakia	Atyp EH w sev OED Anterior maxilla 04/2017	Ulceration	SCC Palatal mucosa & gingival margin 01/2018	5/6 high risk 1/6 low risk
63	**1952**	**M**	**Hyperkeratosis leukoplakia**	**Mod OED** **Lateral posterior tongue** **11/2017**	**Leukoplakia**	**SCC** **Anterior floor of mouth** **07/2018**	**6/6 low risk**
67	1963	F	Leukoplakia	Mod OED Lateral tongue 01/2018	Leukoplakia	Sf-invasive SCC Left tongue 05/2020	5/6 high risk 1/6 low risk
83	1963	F	Leukoplakia	Mild to mod OED Ventral surface tongue 03/2018	Leukoplakia	Sf-invasive SCC left tongue 05/2020	6/6 high risk
80	1959	F	*erythro*-Leukoplakia	Atyp EH w OED Gingiva and mucosa 03/2018	Erythroplakia ulceration	Mod to well diff. SCC Buccal gingiva & mucosa 03/2018	6/6 high risk
90	1945	F	*erythro*-Leukoplakia	Sev OED Buccal gingiva 07/2018	Mass with rolled borders	Well diff. SCC Gingiva 12/2019	6/6 high risk
OED Biopsies without MT							
04	1960	F	Multiple leukoplakia	Mod OED Left upper vestibule 07/2014	Rough leukoplakia	HK w mild OED Buccal gingiva 08/2018	6/6 low risk
02	1967	M	Leukoplakia	Mild OED Lateral tongue 07/2014	Leukoplakia	Mild OED Lateral tongue 06/2018	6/6 low risk
08	1967	M	Leukoplakia	Mild to mod OED Lateral tongue 11/2014	Leukoplakia	Mild OED Lateral tongue 06/2018	6/6 low risk
09	1963	M	*erythro*-Leukoplakia	Mild to mod OED Buccal mucosa	Erythroplakia ulceration	Sev OED Left cheek	6/6 low risk

Table 1 *(Contd.)*

Biopsy information			Initial diagnosis		Follow-up diagnosis		Model prediction
ID	Patient birth year	Sex	Clinical description	Histological diagnosis Location Month/year	Clinical description	Histological diagnosis Location Month/year	ROI-level
				11/2014		10/2018	
10	1951	M	Leukoplakia	Mild to mod OED Lateral tongue 11/2014	Leukoplakia	Mod OED Lateral tongue 02/2018	6/6 low risk
11	1983	F	Leukoplakia	VHK w mild OED Lingual 12/2014	Leukoplakia	VHK w mild OED Lingual 12/2018	6/6 low risk
12	1960	M	Leukoplakia	Mild OED Lateral border tongue 02/2015	Leukoplakia	Mild OED Ventral lateral border 02/2020	6/6 low risk
17	**1982**	**M**	**Not given**	**Mod to sev OED Lateral tongue 06/2015**	**Erythroplakia**	**Mod to sev OED Lateral tongue 01/2021**	**5/6 high risk 1/6 low risk**
20	1940	F	Leukoplakia w hyperkeratosis	VHK w epi atyp Palatal 09/2015	Raised leukoplakia	VHK Apical gingival 11/2021	6/6 low risk
41	1934	F	Multiple leukoplakia	VHK w mod OED Left cheek, buccal & lingual upper left 08/2016	Leukoplakia	Mild OED Left buccal mucosa 11/2020	5/6 low risk 1/6 high risk
50	1936	F	Leukoplakia w ulceration	Mod OED Buccal gingiva 01/2017	Hyperplastic tissue	Mild to mod OED Buccal 06/2019	6/6 low risk
54	**1967**	**M**	**Leukoplakia**	**Mod OED Left tongue 04/2017**	**Leukoplakia**	**Mild to mod OED Lateral tongue 01/2020**	**5/6 high risk 1/6 low risk**
56	1952	M	Leukoplakia	VHK w mod OED Facial mucosa 06/2017	Leukoplakia	HK w epi atyp Edentulous site 04/2020	6/6 low risk
59	1951	F	Granular	Mild OED Marginal gingiva 07/2017	Leukoplakia	HK & acan. w epi atyp Marginal gingiva 08/2019	5/6 low risk 1/6 high risk
62	1942	M	Verrucous leukoplakia	HK & acan. w epi atyp Facial 08/2017	Leukoplakia	HK & acan. w epi atyp Gingival margin 07/2020	6/6 low risk
70	1952	M	Erythroplakia	Mild OED Buccal mucosa 01/2018	*erythro*-Leukoplakia	Mild to mod OED Left buccal mucosa 07/2021	6/6 low risk
86	1956	M	Leukoplakia	Mild OED Palatal vault 04/2018	Leukoplakia	VHK Gingiva 07/2021	6/6 low risk
89	**1957**	**M**	***erythro*-Leukoplakia**	**Sev OED Gingiva papilla 07/2018**	**Rough leukoplakia**	**Sev OED Lingual 03/2021**	**3/6 high risk 3/6 low risk**

HK: hyperkeratosis, VHK: verrucous hyperkeratosis, SCC: squamous cell carcinoma, sf-invasive: superficially invasive, EH: epithelial hyperplasia, acan: acanthosis, atyp: atypic, epi: epithelial, mod: moderate, sev: severe, w: with, diff: differentiated.

quality spectral data. To ensure data reliability, six high-quality ROIs were randomly selected from each biopsy, resulting in a total of 180 representative spectra from thirty OED biopsies, which were combined into one OED FTIR dataset for further analysis. Each spectrum was assigned a class label according to the MT outcome of the corresponding patient (1: with MT; 2: without MT). The class-average spectra of OED with and without MT were then compared to those of benign and OSCC tissues from our previous study to identify spectral differences.

Fig. 2 illustrates an overview of the process, including ROI selection, FTIR image acquisition, spectral preprocessing, HCA clustering, and the extraction of average epithelial spectra.

Model evaluation

We previously developed three discriminant models, PLSDA, SVMDA, and XGBDA, to differentiate average epithelial spectra between eleven OSCC and twelve benign oral tissue biopsies. Based on 10-fold Venetian blinds cross-validation, the PLSDA model achieved 100% sensitivity and specificity, while the

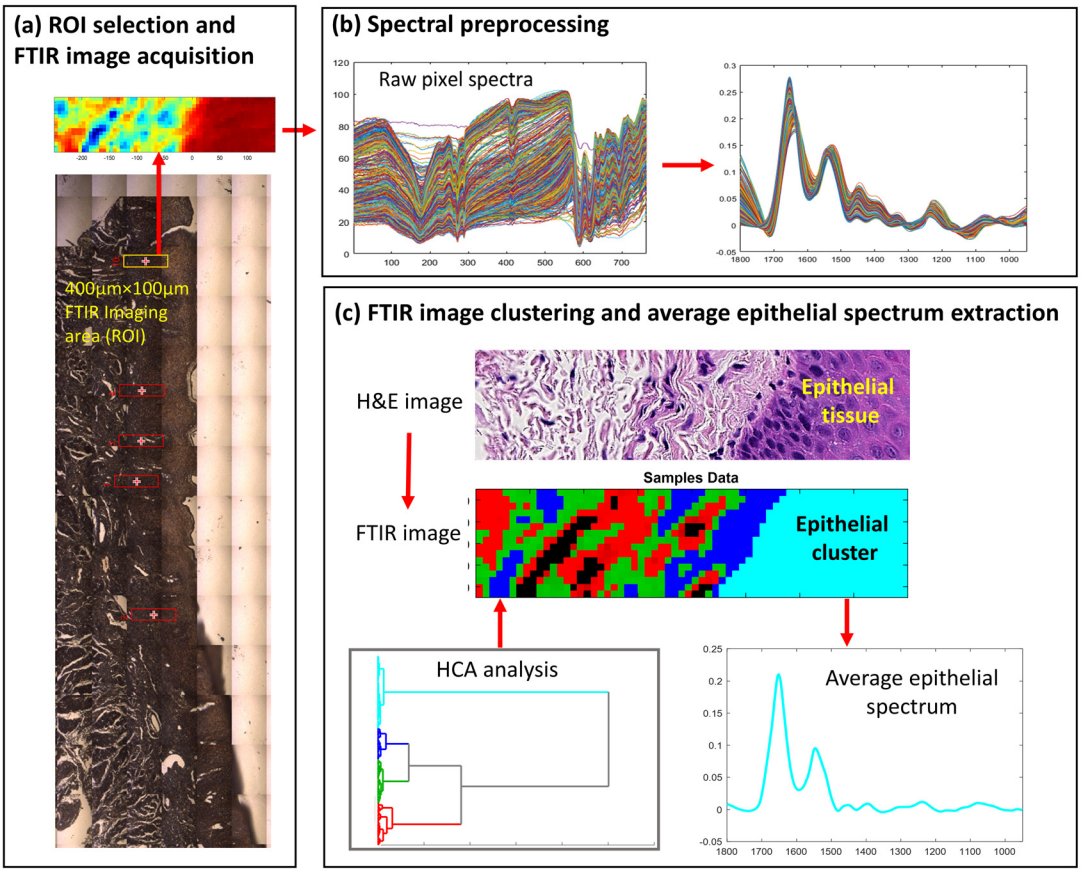

Fig. 2 Illustration of (a) ROI selection and FTIR image acquisition, (b) spectral preprocessing, (c) FTIR image clustering and average epithelial spectrum extraction.

other two models generated 95% sensitivity and 96% specificity.[18] PLSDA is a supervised machine learning technique that extends Partial Least Squares (PLS) regression by incorporating linear discriminant analysis (LDA) for classification. Instead of predicting a continuous response, PLSDA uses a categorical response matrix (Y) to represent class labels. The algorithm identifies latent variables (LVs) from the spectral dataset (X) that best differentiate the classes while maximizing covariance between X and Y. The OSCC-Benign PLSDA model consisted of four LVs, explaining 94.50%, 4.48%, 0.38% and 0.29% of the spectral variance between OSCC and benign tissues, respectively. In the current study, we tested the OSCC-Benign PLSDA model using the OED FTIR dataset to evaluate its performance in predicting MT risk in OED. Under our hypothesis, an OSCC-class prediction indicated high MT risk, while a Benign-class prediction suggested low risk. The dataset contained 72 spectra from twelve OED biopsies with MT and 108 spectra from eighteen OED biopsies without MT, resulting in a class ratio of 40/60 or 2 : 3. Model performance at the ROI level was assessed using ROC (receiver operating characteristic) curves with AUC (area under the curve) scores, confusion matrices, sensitivity, specificity, accuracy, precision, and F1 scores.[21] To determine MT risk at the biopsy level, we applied a majority voting rule: if at least three out of six ROI spectra from a biopsy were classified as high-risk, the entire biopsy was labeled as high-risk. This approach enabled estimation of the OSCC-Benign PLSDA model's predictive performance at the biopsy level.

Meanwhile, we trained another OED PLSDA model using the 180 OED spectra and evaluated its performance. We employed 10-fold Venetian blinds cross-validation for hyperparameter tunning and model performance evaluation. To ensure the rigor of model training and evaluation, we assigned all six spectra from each OED biopsy to a single blind so that they remained together during the split. Model performance at the ROI-level was evaluated using the same metrics as before. However, due to cross-validation and potential variations in ROI-level predictions across iterations, estimating biopsy-level prediction accuracy was not performed. The top four LVs of the OED model were identified and compared to those of the OSCC-Benign model.

Results

Fig. 3 presents a comparison of class average spectra for Benign, OSCC, and OED biopsies with and without MT, highlighting spectral differences mainly in four regions: around

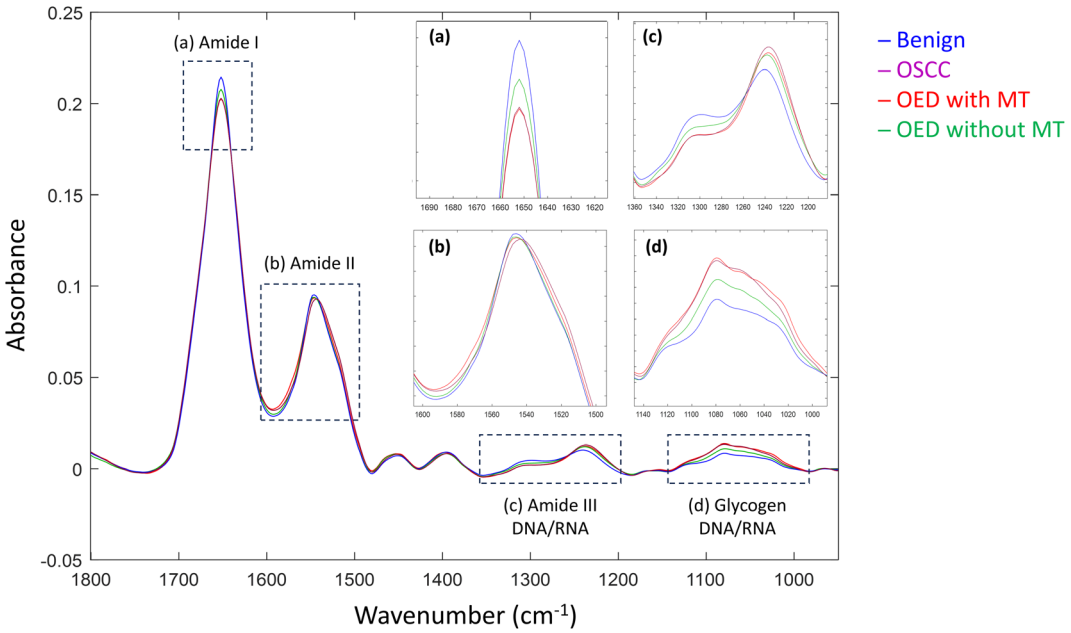

Fig. 3 Comparison of class average FTIR spectra in the fingerprint region (1800–950 cm^{-1}) for Benign, OSCC, OED with and without MT. Inserts show the enlarged spectral regions for (a) Amide I, (b) Amide II, (c) Amide III, DNA/RNA, and (d) Glycogen, DNA/RNA.

1650 cm^{-1}, 1600–1500 cm^{-1}, 1350–1180 cm^{-1}, and 1160–950 cm^{-1}. The 1650 cm^{-1} band corresponds to the amide I band of proteins, mainly associated with C=O stretching vibrations in the peptide backbone. The comparison revealed a descending trend in Amide I band intensity in the order of Benign > OED-without-MT > OED-with-MT/OSCC, with OED-with-MT exhibiting a band intensity closely resembling that of OSCC. The 1600–1500 cm^{-1} region represents the amide II band of proteins, mainly linked to the bending vibration of N–H bond and the stretching vibration of C–N bond in the peptide backbone. The comparison showed a descending band intensity at 1548 cm^{-1} following the order Benign > OED-without-MT > OED-with-MT > OSCC. Additionally, band broadening was observed in the order OSCC/OED-with-MT > OED-without-MT > Begin, along with a red shift toward lower wavenumbers from 1548 cm^{-1} to 1500 cm^{-1}, following the trend OSCC > OED-with-MT > OED-without-MT/Benign. The spectral region of 1350–1180 cm^{-1} is attributed to the amide III band of proteins (1350–1250 cm^{-1}), the asymmetric vibration of $-PO_2^-$ (1240 cm^{-1}) and the deformational modes of the CH_3/CH_2 groups in phospholipids and nuclei acids. The comparison disclosed a descending band intensity at 1310 cm^{-1} in the order of Benign > OED-without-MT > OED-with-MT/OSCC, with OED-with-MT closely resembling OSCC. Similarly, the band at 1240 cm^{-1} exhibited decreasing intensity in the order OSCC > OED-with-MT > OED-without-MT > Benign, accompanied by a red shift in the same order. The spectral region of 1160–950 cm^{-1} is attributed to the stretching vibrations of the C–O/C–C groups in carbohydrates (*e.g.*, glycogen) at 1154 and 1030 cm^{-1}, as well as the symmetric vibration of $-PO_2^-$ in phospholipids and nuclei acids at 1080 cm^{-1}. The comparison indicated a descending band intensity at 1080 cm^{-1} following the order OSCC/OED-with-MT > OED-without-MT > Benign, with OED-with-MT closely resembling OSCC.[12,22–25]

Table 1 summarizes the demographic and diagnostic information for thirty OED biopsies from twenty-six patients. Notably, biopsy pairs #06 and #94, #51 and #55, #67 and #83, and #02 and #08 represent biopsies from the same patients. Among the twenty-six patients, there were an equal number of males and females, with thirteen of each. The patients' ages ranged from 35 to 86 years at the time of their follow-up diagnoses. The time interval between the initial and follow-up diagnoses for the OED with MT ranged from three to fifty-eight months, with one exception. Biopsy #80 had an OSCC diagnosis within one month of the initial OED diagnosis, which may indicate a misdiagnosis due to mis-sampling, as moderate or severe dysplasia may occur near carcinoma. Nonetheless, we retained this biopsy to evaluate whether our approach could identify such misdiagnoses. The time interval between diagnoses for the OED without MT ranged from twenty-five to seventy-four months. The MT risk prediction for each of the six ROIs in the OED biopsies, as determined by the OSCC-Benign PLSDA model, is shown in the last column. Using the majority voting rule, our analysis identified five OED biopsies with incorrect predictions, including two false positives and three false negatives, as indicated by the grey rows in Table 1.

Fig. 4 illustrates the MT risk probability distribution for the 180 OED representative spectra predicted by the OSCC-Benign PLSDA model. Each biopsy is represented by six consecutive markers of the same color and shape. OED spectra with and

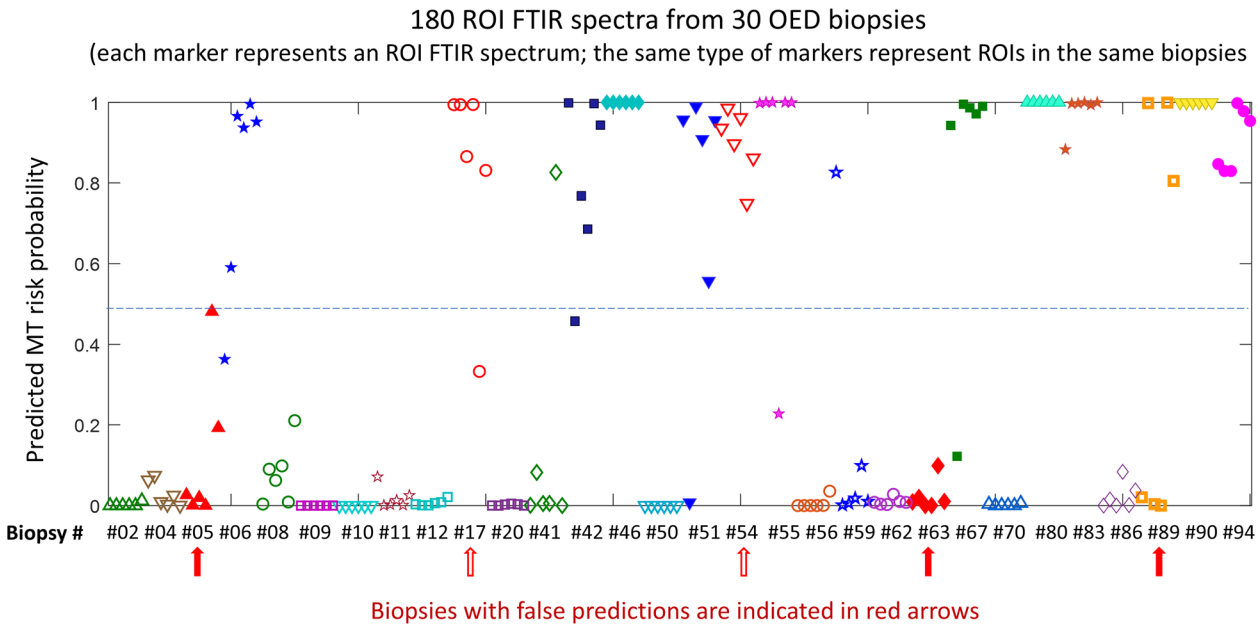

Fig. 4 MT risk probability for 180 representative FTIR spectra from 30 OED biopsies, predicted by the OSCC-Benign PLSDA model. Each biopsy is represented by six consecutive markers in the same color and shape. Red empty and solid arrows indicate false positive and false negative predictions, respectively.

without MT are represented in solid and empty markers respectively. The two false positives and three false negatives are indicated by empty and solid red arrows respectively. Among the thirty OED biopsies, twenty exhibited a homogeneous risk distribution across all six ROIs, nine demonstrated consistent risk predictions for five of the six ROIs. One particular biopsy #89 showed an equal number of high-risk (three) and low-risk (three) ROIs. Based on the predefined majority voting rule, biopsy #89 was assigned as high-risk for MT.

Fig. 5 summarizes the performance of the OSCC-Benign PLSDA model and the OED PLSDA model for MT risk prediction. Fig. 5a shows the ROC curve with AUC score and confusion matrix for testing 180 OED representative spectra using the OSCC-Benign PLSDA model. The AUC score was 0.89, and the confusion matrix indicated a sensitivity of 76.4%, specificity of 85.2%, accuracy of 81.7%, precision of 77.5%, and an F1 score of 0.77 at the ROI level. When applying the majority voting rule, the OSCC-Benign PLSDA model achieved sensitivity, specificity, and accuracy of 83.3%, precision of 76.9%, and an F1 score of 0.8 at the biopsy-level. Fig. 5b shows the cross-validation ROC curve with AUC score and confusion matrix for the new OED PLSDA model. The AUC score was 0.85, and the confusion matrix indicated a sensitivity of 76.4%, specificity of 88.9%, accuracy of 83.9%, precision of 82.1%, and an F1 score of 0.79 at the ROI level. Among the evaluation metrics, both F1 and AUC scores provide insights into a model's accuracy. While the accuracy score indicates the proportion of correct predictions at a particular decision threshold, the AUC provides a broader evaluation of model performance across different thresholds. The AUC is an effective combined measure of sensitivity and specificity, reflecting the inherent validity of a diagnostic test. An AUC score of 0.8–0.9 indicates very good diagnostic accuracy.[26] The F1 score, which combines precision and recall (sensitivity), is particularly useful for evaluating models with imbalanced classes. In the current study, with a class ratio of 2 : 3, the F1 score may provide a more reliable evaluation than the accuracy score. Fig. 5c provides a summary of the performance metrics, including sensitivity, specificity, accuracy, precision, F1 and AUC scores, of the two PLSDA models. For the OED PLSDA model, the Root Mean Square Error of Calibration (RMSEC) was 0.29 and the Root Mean Square Error of Cross-Validation (RMSECV) was 0.39.

Fig. 6 shows the top four LVs of the two PLSDA models in their second derivative format. In the OSCC-Benign PLSDA model, the loadings of LV1, LV2, LV3, and LV4 explained 94.50%, 4.48%, 0.38% and 0.29% of the spectral variations between OSCC and benign tissues, respectively. In the OED PLSDA model, the loadings of LV1, LV2, LV3, and LV4 explained 96.32%, 2.27%, 0.20% and 0.17% of the spectral variations between OED biopsies with and without MT, respectively. A visual comparison shows that LV1 and LV2 are very similar in both models, collectively explaining 99.0% of the spectral variations between OSCC and benign tissues, as well as 98.5% of the spectral variations between OED tissues with and without MT.

Eleven prominent FTIR bands were identified from the top two latent variable loadings (LV1 and LV2) of both PLSDA models as discriminative spectral biomarkers for differentiat-

(a) OSCC-Benign PLSDA Model

ROC with AUC

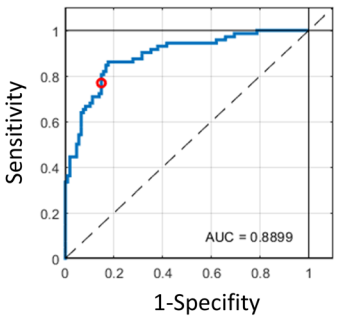

Confusion Matrix

Testing (ROI Level)		
	Predicted Low-Risk	Predicted High-Risk
OED without MT	92	16
OED with MT	17	55

(b) OED PLSDA Model

ROC with AUC

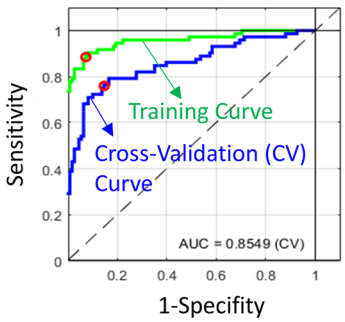

Confusion Matrix

Cross-Validation (ROI Level)		
	Predicted Low-Risk	Predicted High-Risk
OED without MT	96	12
OED with MT	17	55

(c) Performance Metrics for both Models at ROI Level

Model	Sensitivity	Specificity	Accuracy	Precision	F1	AUC
OSCC-Benign PLSDA	76.4%	85.2%	81.7%	77.5%	0.77	0.89
OED PLSDA	76.4%	88.9%	83.9%	82.1%	0.79	0.85

Fig. 5 Model performance in ROC with AUC and confusion matrix for MT risk prediction in OED at the ROI-level for the (a) OSCC-Benign PLSDA model, in which the OED FTIR dataset was used as a test set, and (b) OED PLSDA model, which was trained using the OED FTIR dataset with 10-fold veteran blinds cross-validation. (c) A summary of performance metrics for both models.

ing OED biopsies with and without MT, as summarized in Table 2. These discriminative bands are attributed to alterations in the quantities and molecular structures of proteins (1670 cm^{-1}, 1654 cm^{-1}, 1550 cm^{-1}, 1516 cm^{-1}, 1080 cm^{-1}, 970 cm^{-1}), nucleic acids (1237 cm^{-1}, 1080 cm^{-1}, 970 cm^{-1}), lipids (1704 cm^{-1}, 1482 cm^{-1}), and carbohydrates (1080 cm^{-1}, 1428 cm^{-1}, 1024 cm^{-1}) within the tissues.[12,24]

Discussion

OED is a histologically defined oral lesion that carries an increased risk of progression to OSCC. The primary goal of OED grading is to evaluate tissue abnormalities and assess a patient's risk of malignant transformation. The current gold standard for OED diagnosis is the WHO's three-tier system, which grades dysplastic lesions as mild, moderate, or severe based on histological features. Moderate or severe OED has been shown to be statistically associated with a greater risk of MT compared to mild OED, with an odds ratio of 2.4 (99% CI 1.5–3.8).[27] However, there are several issues with the WHO diagnostic system, including substantial subjectivity and wide inter- and intra-observer variability, especially for moderate OED.[28] To address these issues, Kujan *et al.* proposed a binary grading system that categorizes dysplastic lesions as either low or high grade using morphological criteria similar to those of the WHO system.[29] Although some studies have suggested that the binary system improves observer consistency compared to the three-tier system,[30,31] a recent meta-analysis indicated that both grading systems exhibited limited effectiveness in predicting MT in individual OED patients.[32] In some cases, lower-grade lesions may progress to OSCC, while higher-grade lesions may remain unchanged.[33,34] Additionally, patients without an OED diagnosis may still develop OSCC.[35]

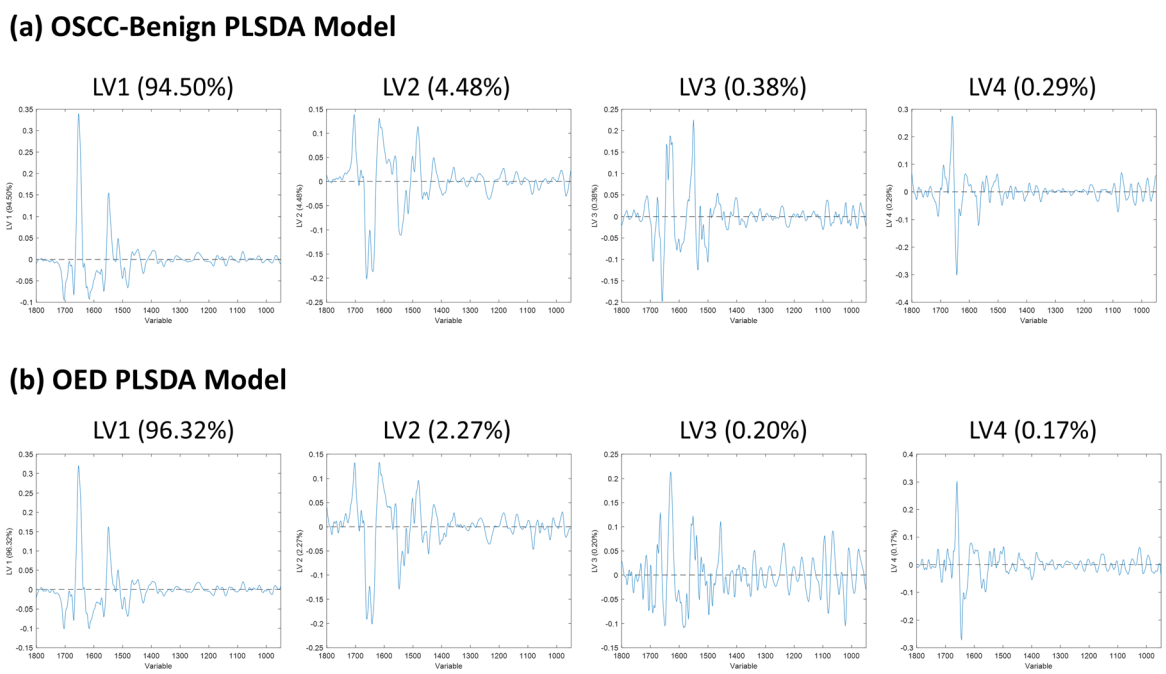

Fig. 6 Comparison of the top four latent variables (LVs) between the (a) OSCC-Benign PLSDA model and (b) OED PLSDA model. The LVs are in second derivative form of the FTIR spectra.

Table 2 Important FTIR spectral biomarkers for differentiating between OEDs with and without MT

Wavenumber (cm^{-1})	Vibrational modes and biochemical assignments
1704	Ester carbonyl C═O stretching, fatty acid esters, lipids
1670	Amide I, secondary structure of proteins
1654	C═O stretching of Amide I
1550	C–N & CN–H stretching of amide II
1516	Amide II, secondary structure of proteins
1482	Deformation vibrations of $-CH_3$, lipid
1428	CH_2 bending (polysaccharides, cellulose)
1237	Asymmetric phosphodiester stretching νas ($-PO_2^-$), lipid, DNA/RNA, Amide III (C–N stretching, N–H bending)
1080	Symmetric phosphodiester stretching *vs.* ($-PO_2^-$), protein phosphorylation, phospholipids, collagen, DNA/RNA
1024	Glycogen (C–O stretching associated with glycogen)
970	C–O stretching of the phosphorylated proteins, DNA/RNA

At the molecular level, it remains unclear why some OED lesions progress to OSCC while others don't, and the mechanisms driving OED progression are still poorly understood.[36] Oral carcinoma is thought to arise from the progressive accumulation of molecular changes, with the final change establishing the cancer genotype and triggering invasion.[37] The process of MT may involve a range of genetic and molecular alterations, including enhanced oncogene activity, reduced tumor suppressor gene function, changes in cell cycle regulators and growth factors, as well as alterations in protein phosphorylation, mitosis, and cell proliferation.[38–41] However, research on genetic changes in dysplastic lesions and OSCC has yielded conflicting results. While some research identified shared genetic changes between dysplastic lesions and carcinoma samples, other studies showed that molecular changes in precancerous lesions had little relationship to those in subsequent carcinomas.[42–45] Many molecular biomarkers have been studied for their potential in predicting MT in OED. These include biomarkers of cell proliferation and apoptosis (*e.g.*, Ki-67 and p53), cell adhesion and junction proteins (*e.g.*, podoplanin and S100A7), immune and inflammatory markers (*e.g.*, CD68 and PD-1), as well as biomarkers associated with genomic instability, cancer stem cells and miRNAs.[46,47] Unfortunately, no single biomarker has demonstrated sufficient clinical reliability for OED diagnosis.[48] Multi-omics approaches offer new opportunities to integrate data across different cellular function levels, including genomics, epigenomics, transcriptomics, proteomics, metabolomics, and microbiomes, to enhance our understanding of complex diseases such as oral cancer and precancerous oral lesions. Despite their promise, clinical translation and implementation of multi-omics approaches face significant challenges, including the need for specialized infrastructure, advanced computational resources, and the high costs associated with data generation and analysis.[49]

We propose the integration of FTIR with machine learning to address the challenges in OED diagnosis. One notable advantage of the FTIR technique is its capability to provide a comprehensive molecular fingerprint of a biological sample,

capturing information across the entire "omics" landscape simultaneously. In a previous study, we applied FTIR to evaluate oral biopsy tissues with histological diagnoses of hyperkeratosis (benign), moderate-to-severe dysplasia, and OSCC. We developed discriminant models that accurately differentiated epithelial FTIR spectra between OSCC and benign tissues. Interestingly, we observed that some OED epithelial spectra closely resembled OSCC, while others were more similar to benign tissue. This led us to hypothesize that the OSCC-like subgroup of OED carries a high risk of MT, while the Benign-like subgroup carries a lower risk. In the current study, we tested this hypothesis by applying the OSCC-Benign PLSDA model to a labelled OED FTIR dataset with documented MT outcomes. The model demonstrated good predictive performance, with a sensitivity of 76.4%, specificity of 85.2%, precision of 77.5%, F1 score of 0.77, and accuracy of 81.7% at the ROI-level. Applying the majority voting rule for each biopsy further enhanced model performance, achieving sensitivity, specificity and accuracy of 83.3%, precision of 76.9%, and an F1 score of 0.8 at the biopsy level. In contrast, the gold standard WHO three-tier system has been reported to provide only 24–40% accuracy in predicting MT in OED.[32,50] Similarly, a meta-analysis of the histological binary grading system showed that the MT rates for low-grade and high-grade OED cases were 12.7% and 57.9%, respectively.[51] When comparing our model's predictions with WHO histological grading, all eight mild OED biopsies were classified as low-risk, while five out of six severe or moderate-to-severe OED biopsies (except for #05) were classified as high-risk for MT. This indicates a strong correlation between histological grading and our model's predictions, particularly for mild and severe/moderate-to-severe OED biopsies. Moderate OED diagnosis presents the greatest challenge within the WHO three-tier system, often exhibiting poor inter-observer agreement and a lack of clear clinical management guidelines (28, 52). In our study, out of the 12 moderate/mild-to-moderate OED biopsies, our model correctly classified ten cases (four high-risk and six low-risk), achieving an accuracy of 83%. This suggests that our FTIR-based machine learning approach could offer a more objective and reliable method for risk assessment and management of moderate OED biopsies.

At the biopsy-level, our model produced two false positives and three false negatives. Specifically, two OED biopsies #05 and #63, from patients with MT, were predicted as low risk. This discrepancy may result from mis-sampling during the initial biopsy procedure or inaccuracy of the model. On the other hand, three OED biopsies #17, #54, and #89 from patients without MT were predicted as high-risk, which may be due to inaccuracy of the model, possible clinical interventions following the initial OED diagnoses, or a potential MT process beyond the follow-up period. Four of the five misdiagnosed biopsies had false predictions from all (6/6) or the majority (5/6) of the ROIs, while one misdiagnosed biopsy (#89) had false predictions from half (3/6) of the ROIs, suggesting biochemical heterogeneity within some OED tissues. Tissue heterogeneity will be the subject of our future studies to better understand how it influences the prognosis and risk assessment of OED.

In the literature, we found two other studies from the same research group that also investigated an FTIR-based machine learning approach for MT prediction in OED. Ellis *et al.* applied principal component analysis followed by linear discriminant analysis (PCA-LDA) to FTIR spectra from 17 OED biopsies and produced a mean sensitivity of 79% and specificity of 76% in MT prediction.[52] The authors subsequently conducted a follow-up study on the same dataset using a different machine learning algorithm (MLA) and generated a mean sensitivity of 84% and specificity of 79% in predicting the MT of OED.[53] Our study differs from these two studies in several key aspects, including sample size (30 *vs.* 17), FTIR instrumentation and acquisition protocols, spectral pre-processing methods, discriminant models (PLSDA *vs.* PCA-LDA and MLA), and the use of average spectra *versus* pixel-level spectra for model training or testing. A particularly significant distinction lies in our model development approach. While the two other studies used the conventional method of splitting their OED spectral dataset into training and test sets, we explored a novel strategy: applying a model trained for OSCC-Benign discrimination to predict OED risk. This novel approach provides a biologically meaningful rationale for OED diagnosis: OED biopsies with biochemical profiles similar to OSCC are associated with a high risk of MT, whereas those resembling benign tissues carry a lower risk. For further comparison, we developed another OED PLSDA model using the 180-spectrum OED dataset and evaluated its performance *via* 10-fold cross-validation. Notably, the two PLSDA models demonstrated similar performance in predicting MT risk in OED. The loadings of the top two LVs of the two models were nearly identical. Comparison of the class average spectra revealed similar spectral features between high-risk OED and OSCC. Our findings suggest that high-risk OEDs share distinct biochemical characteristics with OSCC, reflecting underlying carcinogenic pathways and molecular changes that lead to cancer development in these OED patients.

This pilot study has several limitations. First, the generalizability of the findings is constrained by the small sample size, which was drawn from a single center. Our future studies aim to expand the sample size and include data from multiple centers, which will help enhance the robustness and reliability of our prediction model across a more diverse patient population. Second, we utilized six ROIs per biopsy to capture the spatial distribution of the tissue. However, the manual selection of ROIs may introduce potential bias. Besides, some biopsies exhibited spatial heterogeneity, which we accounted for using a majority voting rule for biopsy-level predictions. To refine this approach, we plan to capture FTIR images of entire biopsy tissues and perform a more comprehensive analysis of the whole-tissue dataset. We will also explore better methods for interpreting and analyzing spatial heterogeneity. Third, this study focused on the PLSDA model, which was the highest performing model in our previous OSCC-Benign study. Moving forward, we aim to investigate more advanced machine learning techniques, including deep learning architectures such as Convolutional Neural Networks (CNNs), to further enhance the

model performance. Deep learning models excel at automatically learning relevant features from complex, high-dimensional data, and often outperform traditional machine learning models, particularly with large datasets. Through these efforts, we aim to establish and validate the FTIR-machine learning approach for clinical applications in OED diagnosis, ultimately contributing to improved patient outcomes.

Conclusions

In summary, our results demonstrate the potential of the FTIR-based machine learning approach as a more accurate tool for predicting MT risk in OED than traditional histological methods. Our FTIR-based PLSDA model generated 83.3% accuracy on the biopsy level in predicting the MT of OED, compared to less than 40% accuracy reported for the histological method. This approach provides a quantitative and objective diagnostic tool with enhanced biological interpretability, assisting clinicians in the assessment and management of OED patients. Low-risk OED patients can follow conservative surveillance protocols and avoid unnecessary medical procedures, while high-risk OED patients can benefit from timely interventions such as surgery, laser therapy, topical chemotherapy, and photodynamic therapy.[54–56] A high-risk classification may also necessitate additional sampling, more frequent follow-ups, and re-examination of other oral regions to ensure comprehensive assessment.[36] In addition to an objective and accurate diagnostic tool, the quality of biopsy, including factors such as size, depth, orientation and fixation, also contributes to reliable OED diagnosis. Early detection of oral cancer at its precancerous stage can significantly reduce their transformation rates and enhance patient survival outcomes.[50,57,58] Future studies should focus on increasing sample size and developing advanced machine learning models to improve diagnostic accuracy. Additionally, validating these models across diverse multicentric cohorts will enhance their generalizability and readiness for clinical translation.

Author contributions

R.W. conceived and designed the study, secured funding, analyzed and interpreted the data, drafted the original manuscript, critically revised the manuscript, and led the project execution. R.S. contributed to sample preparation and data collection. T.G. provided biopsy samples, along with patient demographic and histological diagnostic information. Y.W. co-conceptualized the study, co-secured funding, reviewed and critically revised the manuscript. All authors approved the final version of the manuscript.

Data availability

The authors confirm that the data supporting the findings of this study are available within the article. Raw data that support the findings of this study are available from the corresponding author, upon reasonable request.

Conflicts of interest

The authors declare no conflicts of interest.

Acknowledgements

This work was supported by National Institute of Dental and Craniofacial Research, National Institute of Health, under grant number R21DE032560.

References

1 J. Ferlay, M. Colombet, I. Soerjomataram, D. M. Parkin, M. Piñeros, A. Znaor and F. Bray, *Int. J. Cancer*, 2021, **149**, 778–789.
2 R. L. Siegel, K. D. Miller and A. Jemal, *CA-Cancer J. Clin.*, 2020, **70**, 7–30.
3 L. Pekarek, M. J. Garrido-Gil, A. Sánchez-Cendra, J. Cassinello, T. Pekarek, O. Fraile-Martinez, C. García-Montero, L. Lopez-Gonzalez, A. Rios-Parra, M. Álvarez-Mon, J. Acero, R. Diaz-Pedrero and M. A. Ortega, *Oncol. Rep.*, 2023, **50**, 213.
4 F. D. Shah, R. Begum, B. N. Vajaria, K. R. Patel, J. B. Patel, S. N. Shukla and P. S. Patel, *Indian J. Clin. Biochem.*, 2011, **26**, 326–334.
5 S. Muller and W. M. Tilakaratne, *Head Neck Pathol.*, 2022, **16**, 54–62.
6 S. Shirani, N. Kargahi, S. M. Razavi and S. Homayoni, *Iran J. Med. Sci.*, 2014, **39**, 406–417.
7 S. Warnakulasuriya, J. Reibel, J. Bouquot and E. Dabelsteen, *J Oral Pathol. Med.*, 2008, **37**, 127–133.
8 I. van der Waal, *Med. Oral Patol. Oral Cir. Bucal*, 2014, **19**, e386–e390.
9 M. L. Goodson, P. Sloan, C. M. Robinson, K. Cocks and P. J. Thomson, *Br. J. Oral Maxillofac. Surg.*, 2015, **53**, 831–835.
10 K. Ranganathan and L. Kavitha, *J. Oral Maxillofac. Pathol.*, 2019, **23**, 19–27.
11 A. Celentano, I. Glurich, W. S. Borgnakke and C. S. Farah, *Oral Dis.*, 2021, **27**, 848–880.
12 A. C. S. Talari, M. A. G. Martinez, Z. Movasaghi, S. Rehman and I. U. Rehman, *Appl. Spectrosc. Rev.*, 2017, **52**, 456–506.
13 Z. Movasaghi, S. Rehman and D. I. ur Rehman, *Appl. Spectrosc. Rev.*, 2008, **43**, 134–179.
14 S. Kumar, A. Srinivasan and F. Nikolajeff, *Curr. Med. Chem.*, 2018, **25**, 1055–1072.
15 J. D. Pallua, A. Brunner, B. Zelger, R. Stalder, S. H. Unterberger, M. Schirmer and M. C. Tappert, *Pathol., Res. Pract.*, 2018, **214**, 1532–1538.
16 L. Bel'skaya, *J. Appl. Spectrosc.*, 2019, **86**, 165–188.
17 R. Wang and Y. Wang, *Int. J. Mol. Sci.*, 2021, **22**, 1206.

18 R. Wang, A. Naidu and Y. Wang, *Diagnostics*, 2021, **11**, 2133.
19 S.-F. Chiu, C.-H. Ho, Y.-C. Chen, L.-W. Wu, Y.-L. Chen, J.-H. Wu, W.-S. Wu, H.-K. Hung and W.-F. Chiang, *Medicine*, 2021, **100**, e24934.
20 J. H. Ward Jr, *J. Am. Stat. Assoc.*, 1963, **58**, 236–244.
21 O. Rainio, J. Teuho and R. Klén, *Sci. Rep.*, 2024, **14**, 6086.
22 A. Barth, *Biochim. Biophys. Acta*, 2007, **1767**, 1073–1101.
23 M. J. Baker, J. Trevisan, P. Bassan, R. Bhargava, H. J. Butler, K. M. Dorling, P. R. Fielden, S. W. Fogarty, N. J. Fullwood, K. A. Heys, C. Hughes, P. Lasch, P. L. Martin-Hirsch, B. Obinaju, G. D. Sockalingum, J. Sulé-Suso, R. J. Strong, M. J. Walsh, B. R. Wood, P. Gardner and F. L. Martin, *Nat. Protoc.*, 2014, **9**, 1771–1791.
24 G. Bellisola and C. Sorio, *Am. J. Cancer Res.*, 2012, **2**, 1–21.
25 E. Wiercigroch, E. Szafraniec, K. Czamara, M. Z. Pacia, K. Majzner, K. Kochan, A. Kaczor, M. Baranska and K. Malek, *Spectrochim. Acta, Part A*, 2017, **185**, 317–335.
26 A.-M. Šimundić, *EJIFCC*, 2009, **19**, 203–211.
27 O. Iocca, T. P. Sollecito, F. Alawi, G. S. Weinstein, J. G. Newman, A. De Virgilio, P. Di Maio, G. Spriano, S. Pardiñas López and R. M. Shanti, *Head Neck*, 2020, **42**, 539–555.
28 O. Kujan, A. Khattab, R. J. Oliver, S. A. Roberts, N. Thakker and P. Sloan, *Oral Oncol.*, 2007, **43**, 224–231.
29 O. Kujan, R. J. Oliver, A. Khattab, S. A. Roberts, N. Thakker and P. Sloan, *Oral Oncol.*, 2006, **42**, 987–993.
30 L. Krishnan, K. Karpagaselvi, J. Kumarswamy, U. S. Sudheendra, K. V. Santosh and A. Patil, *J. Oral Maxillofac. Pathol.*, 2016, **20**, 261–268.
31 P. Nankivell, H. Williams, P. Matthews, S. Suortamo, D. Snead, C. McConkey and H. Mehanna, *Oral Surg. Oral Med. Oral Pathol. Oral Radiol.*, 2013, **115**, 87–94.
32 B. S. de Freitas Silva, D. C. R. Batista, C. F. de Souza Roriz, L. R. Silva, A. G. C. Normando, A. R. dos Santos Silva, M. A. G. Silva and F. P. Yamamoto-Silva, *Clin. Oral Invest.*, 2021, **25**, 4329–4340.
33 P. M. Speight, *Head Neck Pathol.*, 2007, **1**, 61–66.
34 A. K. El-Naggar, J. R. Grandis, T. Takata and P. J. Slootweg, *WHO Classification of Head and Neck Tumours*, World Health Organization, Geneva, Switzerland, 2017.
35 S. Silverman Jr., M. Gorsky and F. Lozada, *Cancer*, 1984, **53**, 563–568.
36 E. Odell, O. Kujan, S. Warnakulasuriya and P. Sloan, *Oral Dis.*, 2021, **27**, 1947–1976.
37 C. R. Leemans, P. J. F. Snijders and R. H. Brakenhoff, *Nat. Rev. Cancer*, 2018, **18**, 269–282.
38 K. Ranganath, A. L. Feng, R. A. Franco, M. A. Varvares, W. C. Faquin, M. R. Naunheim and S. V. Saladi, *Cancers*, 2022, **14**, 5581.
39 G. Cervino, L. Fiorillo, A. S. Herford, U. Romeo, A. Bianchi, S. Crimi, C. D'Amico, R. De Stefano, G. Troiano, R. Santoro, L. Laino, G. Laino and M. Cicciù, *Dis. Markers*, 2019, **2019**, 8040361.
40 S. Choi and J. N. Myers, *J. Dent. Res.*, 2008, **87**, 14–32.
41 H. K. Williams, *Mol. Pathol.*, 2000, **53**, 165–172.
42 H. M. Wood, C. Conway, C. Daly, R. Chalkley, S. Berri, B. Senguven, L. Stead, L. Ross, P. Egan, P. Chengot, J. Graham, N. Sethi, T. K. Ong, A. High, K. MacLennan and P. Rabbitts, *J. Pathol.*, 2015, **237**, 296–306.
43 C. S. Farah, M. Jessri, N. C. Bennett, A. J. Dalley, K. D. Shearston and S. A. Fox, *Oral Oncol.*, 2019, **96**, 42–50.
44 R. Veeramachaneni, T. Walker, T. Revil, A. Weck, D. Badescu, J. O'Sullivan, C. Higgins, L. Elliott, T. Liloglou, J. M. Risk, R. Shaw, L. Hampson, I. Hampson, S. Dearden, R. Woodwards, S. Prime, K. Hunter, E. K. Parkinson, J. Ragoussis and N. Thakker, *Sci. Rep.*, 2019, **9**, 11992.
45 E. Makarev, A. D. Schubert, R. R. Kanherkar, N. London, M. Teka, I. Ozerov, K. Lezhnina, A. Bedi, R. Ravi, R. Mehra, M. O. Hoque, I. Sloma, D. A. Gaykalova, A. B. Csoka, D. Sidransky, A. Zhavoronkov and E. Izumchenko, *Cell Death Discovery*, 2017, **3**, 17022.
46 M. Crawford, E. H. Johnson, K. Y. P. Liu, C. Poh and R. Y. L. Tsai, *Cells*, 2022, **11**, 1033.
47 P. M. Speight, S. A. Khurram and O. Kujan, *Oral Surg. Oral Med. Oral Pathol. Oral Radiol.*, 2018, **125**, 612–627.
48 X. Cai, J. Zhang, H. Zhang and T. Li, *J. Zhejiang Univ., Sci., B*, 2023, **24**, 868–882.
49 O. Menyhárt and B. Győrffy, *Comput. Struct. Biotechnol. J.*, 2021, **19**, 949–960.
50 H. M. Mehanna, T. Rattay, J. Smith and C. C. McConkey, *Head Neck*, 2009, **31**, 1600–1609.
51 F. Yan, P. D. Reddy, S. A. Nguyen, A. C. Chi, B. W. Neville and T. A. Day, *Eur. Arch. Oto-Rhino-Laryngol.*, 2020, **277**, 2967–2976.
52 B. G. Ellis, C. A. Whitley, A. Triantafyllou, P. J. Gunning, C. I. Smith, S. D. Barrett, P. Gardner, R. J. Shaw, P. Weightman and J. M. Risk, *PLoS One*, 2022, **17**, e0266043.
53 J. Ingham, C. I. Smith, B. G. Ellis, C. A. Whitley, A. Triantafyllou, P. J. Gunning, S. D. Barrett, P. Gardener, R. J. Shaw, J. M. Risk and P. Weightman, *IOP SciNotes*, 2022, **3**, 034001.
54 I. van der Waal, *Oral Oncol.*, 2010, **46**, 423–425.
55 S. I. Kvaal and T. Warloe, *J. Environ. Pathol., Toxicol. Oncol.*, 2007, **26**, 127–133.
56 Z. Wang, R. Polavaram, C. F. Fuentes and S. M. Shapshay, *Arch. Otolaryngol., Head Neck Surg.*, 2003, **129**, 869–873.
57 S. Warnakulasuriya, N. W. Johnson and I. van der Waal, *J Oral Pathol. Med.*, 2007, **36**, 575–580.
58 S. Silverman Jr., A. R. Kerr and J. B. Epstein, *J. Cancer Educ.*, 2010, **25**, 279–281.